

Production and performance of multilayer coated conical x-ray mirrors

Melville P. Ulmer

Dept. of Physics & Astronomy, Northwestern University

2131 Sheridan Rd, Evanston, IL 60208-2900, USA

m-ulmer2@northwestern.edu

Robert Altkorn

Dept. of Physics & Astronomy, Northwestern University

2145 Sheridan Road, Evanston, IL 60208, USA

ralkorn@northwestern.edu

Michael E. Graham

Department of Materials Science and Engineering, Northwestern University

2225 North Campus Drive, Evanston, IL 60208-3108, USA

mgraham@northwestern.edu

Anita Madan¹

Advanced Coating Technology Group, Northwestern University

1801 Maple Avenue, Evanston, IL 60201-3140, USA

¹Current Address: IBM Characterization and Analysis, Dept. LUED, 1580 Route 52, East Fishkill, NY 12533-0999

madaanit@us.ibm.com

Yong S. Chu

Advanced Photon Source, Argonne National Lab.

9700 S. Cass Avenue, Argonne, IL 60439, USA

ychu@aps.anl.gov

A method of fabricating replica figured x-ray optics with integral multilayer coatings is presented. Termed the “Intact Electroform Multilayer Process” (IEMP), this technique involves sputtering multilayers onto a reusable super-polished mandrel, electroforming nickel over the multilayers, and removing the multilayer-coated nickel shell intact from the mandrel. This approach offers advantages over more traditional original and segmented-replica fabrication techniques, including low cost, compatibility with a wide range of mirror designs, diameters, and focal lengths, simple integration with multilayer sputtering processes, and the ability to produce complete shells of revolution. The fabrication of W/Si multilayer coated 10 cm diameter conical x-ray mirrors is described, as are reflectivity measurements at 10 and 30 keV. The measured reflectivity of the IEMP multilayers at the 10 keV primary Bragg peak was 17%. Measurements of multiple points on the cone showed multilayer uniformity to within a few percent around the mirror. © 2003 Optical Society of America

OCIS codes:

(0340.0780) X-ray optics : X-ray mirrors

(0340.6720) X-ray optics : Synchrotron radiation

(0310.1860) Thin Films : Deposition and fabrication

(0350.1260) Other areas of optics : Astronomical optics

1. Introduction

Hard x-ray ($\gtrsim 10$ keV) astronomy remains in its infancy because of the lack of focusing optics in this energy range. All instruments developed to date for observations above 10 keV have been based on passive collimator (OSSE¹) or coded aperture² techniques. However it is widely agreed that a number of fundamental astrophysical questions can be addressed only through the increased resolution and sensitivity provided by focusing telescopes combined with position sensitive detectors. Among focusing systems, those having better angular resolution are more desirable as: (a) smaller focal spot size of point sources provides higher signal to background ratio and (b) complex images of extended objects, such as the Crab Nebula, show interesting features down to the limit of current X-ray telescopes (0.5 arc seconds).³ However even far more modest resolution would be of great benefit. (For example the electroformed *XMM-Newton* mirrors achieved 15 arc second resolution.⁴) Some of the issues that could be addressed with a system having better than or equal to 30'' angular resolution include:

1. The active galactic nuclei (AGN) paradigm. This is a topic of great interest not only because of the inherently interesting physics surrounding massive black holes,

but also because the study of AGNs couples to the origin and evolution of galaxies. How the black hole at the center of the AGN evolves and accretes material is not well understood. Measurements in the ~ 40 to 100 keV range would allow us to distinguish between more thermal-like spectra such as NGC 4151⁵ and those dominated by power law components, e.g. 3C 273 and EGRET blazars in general (cf. ref. 6 and references therein). Detecting and classifying such systems will take us a step closer to determining viable physical models of these objects.

2. Supernovae (SNe). SNe and SNe-light curves have taken on increased importance as they are now being used as cosmic distance indicators to measure the cosmological constant, Λ . Current models^{7,8} predict that ^{44}Ti , which has a half life of approximately 70 years and emits at 67.8 and 78 keV, should be detectable from SN remnants that have been produced in the past few hundred years. Although ^{44}Ti is not a major source of energy for type SN Ia light curves (cf. ref. 7), ^{44}Ti emission measurements will be useful in verifying models of these objects (cf. ref. 9). Also, SN are thought to produce cosmic rays (cf. ref. 10,11,12) and measuring the non-thermal hard x-ray radiation from supernova remnants (SNRs) will allow us to measure the cosmic ray population in young SNRs.

3. Pulsars. SNe produce pulsars which emit in the hard X-ray region. Pulsars may explain the origin of the diffuse ~ 50 keV to 100 keV emission seen from the galactic plane (cf. ref. 13). It is known that many more pulsars than have currently been detected must be producing hard X-rays.^{14,15} A focusing telescope capable of detecting these pulsars will enable the development of models of hard X-ray emission versus pulsar magnetic field, period, and orientation with respect to the Earth. These

data would ultimately allow us to confirm or deny the proposition that pulsars produce the diffuse emission from the Galactic plane. The data would also allow us to use pulsar birth rates to derive the origins of the properties of pulsars we see today by estimating the spin and magnetic field of pulsars at birth. The best direct evidence for the strength of pulsar magnetic fields comes from the measurement of cyclotron absorption features near 30 keV in X-ray binary systems. About 10 such systems are known (cf. ref. 16 and references therein), but with a new sensitive instrument, this number should be increased dramatically, thereby providing a sufficiently large sample to relate magnetic fields to models of the accretion flow and X-ray emission.

4. Soft gamma ray repeaters (SGRs). There exist pulsars with fields as large as $\sim 10^{14}$ G that emit in the soft gamma-ray region.^{17, 18, 19} Measuring the X-ray emission from SGRs in their quiescent state will give us a better view of the dependence of the hard X-ray emission on the magnetic field and more data toward understanding the physics of these bizarre objects.

To address these and related problems, several groups around the world have begun to develop optical technologies aimed at providing high resolution imaging in the hard x-ray region. A telescope based on original mirrors (similar to Chandra²⁰) coated with hard x-ray reflecting multilayers could provide a relatively straightforward solution but would be prohibitively expensive. Therefore all efforts to date have been directed toward developing a telescope based on replica optics. The majority of this work has involved segmented slumped glass²¹ or foil mirrors coated with multilayers after figuring.²² Here we describe an alternate approach in which the multilayers are deposited onto mandrel, coated with a structural layer of electroformed nickel, and

subsequently removed intact from the mandrel along with the nickel shell. We believe that this approach offers several advantages, including the simplicity of mounting offered by full shells of revolution and the straightforward extension to complex (e.g. Wolter I) figures. In previous work,²³ we demonstrated feasibility of this “intact electroforming multilayer process” (IEMP) of mirror replication, but achieved only poor reflectivity. We have subsequently improved the process to the point where we can report reflectivity that is realistic for consideration in a hard x-ray telescope.

2. Mirror Fabrication

A schematic of the key components of the IEMP process is shown in Figure 1. We began with a conical electroless-nickel-coated aluminum mandrel (approximately 10 cm diameter \times 10 cm long, with a 0.5 degree draft angle, where draft angle is defined as the angle between the optical axis and surface of the mirror), that was designed by Radiation Science Inc. (Belmont, MA), and fabricated by Hyperfine Inc. (Boulder, CO). The surface roughness of the mandrel was estimated by the manufacturer to be approximately 1–3 nm rms in the 100 μ m- 1mm spatial wavelength range. After polishing by the manufacturer, the mandrel was sent to Northwestern University, where it was coated with a reactively sputtered layer of amorphous carbon nitride (CN_x). CN_x is hard, lubricious coating now ubiquitous in the computer hard disk industry. It was used here to protect the mandrel through multiple replication operations and reduce high spatial frequency surface roughness.^{23,24}

The mandrel was coated in a dual cathode, unbalanced magnetron reactive sputtering system. The chamber is a water-cooled stainless steel box (81 cm \times 81 cm \times 81

cm) with two side doors, on which the cathodes are mounted. The cathodes are 13 cm \times 38 cm rectangular constructions and face one another across the chamber (30 cm apart). They are powered by Advanced Energy 10 kW (max) dc supplies, connected through SPARC-LE V units to minimize arcing. The magnet arrays (behind the targets) are set up so that the unbalanced magnetic field lines close (connect north to south) across the chamber, and thus, promote a high-density plasma in the vicinity of the substrate when a bias is applied to the substrate during sputter deposition. There is a 15 cm diameter rotating substrate table, centered between the targets, so that the distance from target to substrate is 8 cm. The table has water-cooled power connections and can be biased with either dc or rf power. It has a variable speed control operating from 0 to 20 rpm. The sputtering gas (argon) and reactive gases such as nitrogen are brought into the chamber and controlled through mass flow controllers (MFC). A mass spectrometer signal is used in an automatic feed back loop to control the flow of the reactive gas to maintain a preset partial pressure of the gas. A capacitive manometer gage is used to monitor chamber pressure, and a closed loop feed back to the argon MFC is used to maintain a constant pressure during deposition. The deposition temperature is generally less than 200° C, since it is solely a by-product of the process. No auxiliary heating was supplied. The CN_x coating was sputtered from a pyrolytic carbon target in the presence of a controlled partial pressure of nitrogen (up to 1 mTorr) at a total process pressure in the range of 4-6 mTorr. The dc power on the target was typically 2 – 3 kW, and the sputtering rate was in the range of 10 to 20 nm/min. The CN_x is deposited with compressive stress, the magnitude of which depends on composition and the substrate bias level. The

bias level has a particularly strong effect, and dc levels from 0 – 200V (neg.) were tried. Stresses can reach several GPa with a few hundred volts, and our goal was to maintain the level at less than 1 GPa to minimize the possibility of delamination. The bias level also affects the hardness of the deposited film. An rf bias was used, inducing a dc level in the range –30 to –60V on the substrate, to achieve the best combination of hardness and low stress. The final thickness of the CN_x was about 500 nm. The hardness couldn't be measured directly, but is expected to be in the 10 – 20 GPa (\sim 1000 - 2000 Vickers) range. This can be compared to hard chrome plating, which has a hardness of about 10 GPa (\sim 1000 Vickers), or to sapphire with a hardness of 25 GPa (\sim 2500 Vickers). The deposit stress (measured through curvature of Si wafers) was less than 1 GPa (compressive). The coating is uniform along the length of the mandrel since the cathode length is nearly 40 cm compared to the mandrel height of 10 cm. The mandrel is approximately centered relative to the center line of the targets to maximize the uniformity in the axial direction. In addition to providing a hard surface that will be durable and reusable, the CN_x also enhances the smoothness of the mandrel surface. The amorphous nature of the CN_x and the rotation during deposition combine to achieve this beneficial effect. In the nanometer range, the effect can be to reduce the roughness by a factor of two. Optical profiler (Micromap Corp., Tucson AZ Model 512) measurements of the CN_x -coated mandrel indicated that the surface roughness had been reduced to approximately 0.8–1.1 nm rms in the 100 μ m-1mm range.²⁵

After CN_x coating, the replication operation began with the deposition of a copper (\sim 50 nm thick) release layer onto the mandrel. This was performed in a separate

evaporation system, set up to handle the mandrel and to rotate it during evaporation to obtain uniform coatings. After evaporation of the release layer, x-ray reflective tungsten-silicon multilayers (W/Si) were deposited in the dual-cathode sputtering chamber, configured with a W target on one side and Si on the other. The film structure is controlled by a.) target power (individual layer thickness), b.) rotation rate of the table (bi-layer period), and c.) substrate bias (internal stress and film density). The process pressure was again held constant at 4 mTorr of argon. The power on the targets was in the range of 0.25-1.0 kW for the tungsten and 2-3 kW for the silicon. The stress levels were of concern, so stress was adjusted through preliminary depositions on Si wafers followed by measurements of wafer curvature and stress calculation using modified Storey's equation. Ultimately the bias was minimized to keep the stress under 1 GPa, but at a level that would provide good film density and interface smoothness. RF bias was again used, and a dc level (induced) of 0-10V (negative) was found to be best. A nanolayer structure was produced consisting of 60 bilayers with a bi-layer period of about 5 nm. It is important in this layered construction to minimize any interfacial roughness, in order to achieve the best reflectance (coherency) for the x-rays. We believe that the use of some low level bias, and in particular the rf power, enhances the desired smoothing effect. The bias-induced ion bombardment supplies energy to the growing film in the form of adatom mobility, which helps to minimize the surface energy/roughness of the film. In addition to mandrels, several small Si wafers were coated with multilayers for comparison purposes. These wafers were mounted on a support having the same shape and thermal mass as the mandrel and coated using the same deposition conditions.

Following deposition of the multilayers, the mandrel was returned to the evaporation chamber and coated with thin layers of Cr followed by Au to promote adhesion to electroformed nickel. It was subsequently coated with a structural (~ 0.6 mm) layer of nickel in a low stress nickel sulfamate electroforming bath. The nickel deposit stress was adjusted to be slightly tensile, and the coated replica mirror (nickel through copper layers) was separated from the CN_x -coated mandrel after cooling from plating bath temperature (~ 45 C) to room temperature. The copper was then removed with aqueous $\text{Fe}(\text{NO}_3)_3$, leaving a nickel shell internally coated with multilayers and a CN_x -coated mandrel ready for additional replication operations. A photograph of a multilayer-coated replica mirror is shown in Figure 2.

3. Mirror Characterization

A. X-ray Scans

Two conical Si/W-multilayer-coated IEMP replicas were selected for optical and x-ray analysis. The first was cut to form several small pieces that were characterized using a laboratory diffractometer with a fixed-tube-x-ray source (Cu $k\alpha$ line at 8.4 keV), which indicated the multilayer d-spacing to be 5.3 nm. The second (complete intact) mirror along with the pieces cut from the first mirror were then taken to the Advanced Photon Source (APS) at Argonne National Laboratory where x-ray reflectivity measurements were performed at 10 and 30 keV.

Synchrotron reflectivity measurements proved complicated because of figure error (slope errors corresponding to ~ 1 degree over 1 cm) in the IEMP mirrors subsequently traced to corresponding error in the mandrel.²⁵ These X-ray measurements

were performed using a standard reflectivity setup at the 2-BM-B bending magnet beamline. The incident beam defined by the slits was 0.1 mm (vertical) by 2 mm (horizontal), and the reflected beam was measured using a NaI x-ray scintillation detector with acceptance angles of 1.5 mrad (vertical) x 15 mrad (horizontal).

The IEMP mirror was mounted at the center of the diffractometer by first aligning the mirror surface parallel to the direct x-ray beam and subsequently adjusting the mirror height to bisect the beam. Specular x-ray reflectivity measurements were made by maintaining the momentum transfer wave vector, q , normal to the surface while varying the magnitude of q . In practice, this radial scan was carried out by performing a 2θ - θ scan in which the scattering angle of the x-ray beam (designated 2θ) was scanned at a rate twice that of the incident grazing angle to the mirror surface (designated θ). Before each measurement, the curvature of the mirror axis was aligned to the incident beam using the χ and ϕ motions of the diffractometer so that the optical axis of the mirror was in the scattering plane. In order to check the homogeneity of the deposited multilayers, the mirror was rotated about its optical axis and the measurement repeated. At each rotation angle specular reflectivity was measured at 10 and 30 keV in order to distinguish between the scattering from the multilayers (which scales with the energy of the incident beam) and scattering caused by sample figure error and other possible geometrical effects (which are energy independent). The values of 10 and 30 keV were chosen for experimental simplicity. The 10 keV photons were selected using the Si(111) reflection from a Si double monochromator combined with a 20-keV-cutoff Cr harmonic rejection mirror. The 30 keV photons were selected using the 3rd order harmonic of the Si(111) mirror without changing

the monochromator setting in combination with a 32-keV-cutoff Pt harmonic rejection mirror and Pb attenuators sufficient to effectively remove the 10 keV x-rays with minimal attenuation at 30 keV. Additional rejection of 10 keV x-rays was carried out by electronic discrimination of 10 keV signals from the NaI detector.

The 30 keV measurement (Figure 3) demonstrates that the multilayers perform in the energy range desired for astronomical applications range. Unfortunately figure error in the mandrel was sufficient to prevent direct measurement of absolute reflectivity; however a reflectivity range can be inferred from available data. Figures 4a and 4b show 10 keV reflectivity at two rotated positions of the mirror. These results represent a significant improvement over our previous work.²³ The dashed curves are were generated by IMD²⁶ using a model of 60 Si/W layers with the Si and W layer thicknesses of 4.229 nm and 1.062 nm, respectively. In order to explain the successive suppression of second and third order multilayer peaks, 0.6 nm multilayer inter-diffusion/roughness was included in the model.

B. X-ray imaging

To determine the absolute reflectivity at the primary 10 keV Bragg peak, we used a small (1.2 cm along the optical axis x 3 cm perpendicular to the optical axis) segment from the first mirror. We anticipated that this segment would be small enough to avoid figure errors in the optical axis direction; however this was not the case. Therefore we carried out diffuse scattering measurements with a CCD imaging system in order to investigate further the effect of figure errors on our x-ray measurement. The CCD pixels are 9 microns square, and the direct beam was set to 3 mm (horizontal) x 50

microns (vertical). The CCD was mounted on the two-theta arm of the diffractometer 45 cm from the center of the mirror segment. The angular position of the CCD on the diffractometer arm was adjusted such that diffuse one CCD exposure subtended the two-theta angular range of -0.5 to 3.0 degrees. Fig. 5 shows the image obtained from the CCD at a fixed incident X-ray angle of 0.7 deg, which corresponds to the incident angle of the 1st order multilayer reflection as shown in Figures 4a and 4b. For a qualitative assessment we averaged the CCD data perpendicular to the scattering plane and superposed the resulting plot of the average intensity versus 2θ on the CCD image (see Figure 5).

If the surface were completely flat, only the 1st order reflection at 1.4 deg would be seen in CCD image. *The units used here are 2θ ; therefore divide by 2 to compare with Figures 3 and 4.* Our measurement, however, revealed a much more complex intensity distribution. In addition to the 1st order reflection at 1.4 deg (cf. the top scale in Figure 5), a distribution of intensities below ~ 1.1 deg was observed. In particular, irregular patterns of intensity streaks running horizontally are clearly visible in this angular range. We attribute this extra intensity distribution to the figure error of the mirror surface. As schematically shown in the inset of Fig. 5, the angle between the parallel x-ray beam and the various position of the mirror surface can severely deviate from the "average mirror surface". Consequently, the scattering intensity originating from different parts of the mirror fluctuate significantly due to the figure errors. The intensity below 0.1 deg is due to the various effects including the partial eclipsing of the diffuse scattering from air in the path of the beam due to the sample and the scattering from the region near the tip of the sample closest to the CCD.

In order to further investigate the effects of the figure error on the diffuse scattering CCD image, we took a series of CCD image of the diffuse scattering as a function of the "average" incident angle and verified the following facts. First, the 2D diffuse scattering intensity distribution below 1.1 deg is highly sensitive to the incident angle. At lower incident angles, the intensity fluctuation and the visibility of the streaks increased, further confirming our conclusion this excess intensity originate mostly from the figure errors of the mirror surface. Second, the 1st order multilayer peak at 1.4 deg was observed over a wide range of the incident angles (almost over 1 deg range). Third, the diffuse scattering due to the figure errors were observed to sharply decrease with the increasing scattering angle and no significant intensity was observed above 1.1 deg.

C. Optical Profiler Figure Measurements

The figure error inferred from in the X-ray measurements was qualitatively (it is beyond the scope of this work to perform detailed ray tracing analysis) verified by the figure error measurements performed on the segment used in the experiment to produce Figure 5 by Takacs.²⁵ Takacs used an optical profiler Micro Map 200 with 2.5 X objective. The optical profiler measurement produced a 2 dimensional 640×160 matrix readout of height as function of position with approximate 5×5 micron pixel resolution and height measurement on a scale with sub-micron accuracy. In Figure 6 we show the variation in height of the mirror segment along the optical axis. This plot is based on the data averaged over a 55 micron wide strip in the direction perpendicular to the optical axis. In Figure 6 a typical "ripple-like" structure is seen

which is similar to the schematic inserted in Figure 5. This structure is attributable to the mandrel, *not the mirror fabrication process*, since measurements of the mandrel made by Takacs²⁵ with the same Micro Map system gave similar results to those shown in Figure 6.

D. Interpretation of Results

Having understood the origin of the "geometric" effects in our x-ray study, we proceed to determine the overall efficiency of the entire mirror. The problem with the using the integrated peak intensity as determined by the conventional radial scan as shown in Fig. 3-4 is that the exact fraction of the surface contributing to the measured intensity is unknown due to the extensive figure error. At different incident angles, different parts of the mirror contribute to the intensity of the 1st order reflection. Thus, the only way to defeat this problem is to rock the incident angle over a wide range so that the integrated intensity from all parts of the mirror can be obtained. Since the CCD lacked the dynamic range required for the measurement, we used the NaI scintillation detector to carry out the rocking scan of the incident angle with the fixed scattering angle at 1.4 deg (i.e. transverse scan). The measurement yielded a wide intensity profile with a full-width-half-max of 0.8 degree. This is consistent with both the CCD diffuse scattering and the profilometry measurements. We can ignore the background contribution to this measurement, because we have already verified that the diffuse scattering intensity due to the figure errors was absent around the 1st order reflection at 1.4 deg. In addition, there was no need to perform the radial scan, because the detector vertical angular acceptance of 1.5 mrad was much larger than the radial

width of the 1st order peak of 0.04 deg (FWHM). This integration procedure of the 1st order reflection yielded 17% absolute reflectivity at 10 keV. Given the shadowing effect of the ripple structure, this could even be an underestimate. As a cross check of the derived absolute reflectivity efficiency, we also measured the reflectivity of a flat W/Si-multilayer coated Si sample fabricated under same conditions as the figured mirrors. The efficiency of first Bragg reflectivity that we measured from this sample was $16 \pm 5\%$.

4. Conclusions and Summary

Based on comparisons between the data and a single-d-spacing IMD model, we conclude that d-spacing of the IEMP multilayers are uniform to approximately 1% both around the cylindrical azimuth of the mirror and as a function of depth. We used exactly the same d-spacing to fit the two 10 keV measurements made at different rotational positions about the optical axis of the mirror and to model the much more penetrating 30 keV X-ray results. The intensities and widths of the first three multilayer Bragg peaks agree well with the single-d-spacing model, further supporting a high degree of uniformity along the depth of the multilayer. If the multilayer had a large deviation of d-spacing around its average value along the depth, the intensity of the higher order Bragg peaks would have fallen much more rapidly in the same fashion as a crystal with a very large Debye-Waller factor. In addition, the decrease in intensity would have been much more apparent at 30 keV if the d-spacing of the multilayer had fluctuated along the depth. Consequently, it would have been difficult to model both data sets with the same parameters.

As noted in the previous section, the absolute reflectivity of the complete IEMP mirror was difficult to determine from a simple 2θ - θ scan, since geometrical (figure error) effects clearly affected the reflectivity measurements. For example, the extra intensities in Fig. 3 and Fig.4 left of the 1st order reflection, as confirmed by the CCD measurements in Fig. 5, are due to the figure errors of the mirror surface in which various parts of the sample reflect the incident at different scattering intensities. In order to properly estimate the overall efficiency of the multilayer mirror it was necessary to overcome effects due to the figure errors. To do this, we resorted to a transverse scan through the 1st order reflection, integrating the Bragg reflection from all parts of the sample. Consequently, we determined an absolute reflected intensity of approximately 17% at 10 keV.

In summary, we have shown there are technical reasons as well a strong astrophysical motivation for developing the technology to make mirrors that are coated with multilayers using the IEMP. We have demonstrated that the IEMP is viable by measuring the reflectivity of a mirror made by this process at both 10 keV and 30 keV. The results indicate highly efficient reflectivity at the primary Bragg peaks (well above 10%) from 60 Si/W multilayers.

5. Acknowledgments

This work was supported in part by NASA grant NAG5-5094. We thank Prof. Yip-Wah Chung (Northwestern University) for advice, and Dr. Derrick C. Mancini and the rest of the Argonne National Lab APS SRI-CAT for support and providing us access to the 2-BM-B beam-line. The use of APS was supported by the U.S. Department of

Energy (DOE), Basic Energy Sciences (BES), Office of Science, under Contract No. W-31-109-Eng-30. We thank Drs. Allen S. Krieger and Daniel Parsignault (Radiation Science Inc.) for providing the mandrel. We thank Mr. Matthew Steele (Northwestern University) for fitting the X-ray reflectivity data with the IMD code. We thank Dr. Peter Z. Takacs (Brookhaven National Laboratory) for making the optical profiler measurements.

References

1. W. N. Johnson, R. L. Kinzer, J. D. Kurfess, M. S. Strickman, W. R. Purcell, D. A. Grabelsky, M. P. Ulmer, D. A. Hillis, G. V. Jung, R. A. Cameron, “The oriented scintillation spectrometer experiment - Instrument description”, *Ap. J. Suppl.* **86**, 693–712 (1993).
2. F. Lebrun, and J. Paul, “The main lessons from the SIGMA mission for the future of hard x-ray and soft gamma ray instrumentation for astronomy”, in *EUV, X-ray, and Gamma-Ray Instrumentation for Astronomy III*, O. H. W. Siegmund, ed., Proc. SPIE **1743**, 155-161 (1992).
3. J. J. Hester, K. Mori, D. Burrows, J. S. Gallagher, J. R. Graham, M. Halverson, A. Kader, F. C. Michel, and P. Scowen, “Hubble Space Telescope and Chandra Monitoring of the Crab Synchrotron Nebula”, *Ap. J. (Letters)* **577**, L49-L52 (2002).
4. B. Aschenbach, “In-orbit performance of the XMM-Newton x-ray telescope: images and spectra”, in *X-Ray Optics for Astronomy: Telescopes, Multilayers, Spectrometers, and Missions*, P. Gorenstein and R.B. Hoover Eds., Proc. SPIE **4496**,

- 8-22 (2002).
5. A. A. Zdziarski, W. N. Johnson, and P. Magdziarz, “Broad-band gamma-ray and X-ray spectra of NGC 4151 and their implications for physical processes and geometry”, *M. N. R. A. S.* **283**, 1993–206 (1996).
 6. R. Mukherjee R, D. L. Bertsch, S. D. Bloom, B.L. Dingus, J. A. Esposito, C. E. Fichtel, R. C. Hartman, S. D. Hunter, G. Kanbach, D. A. Kniffen, Y. C. Lin, H. A. MayerHasselwander, L. M. McDonald, P. F. Michelson, C. vonMontigny, A. Mucke, P. L. Nolan, M. Pohl, O. Reimer, E. Schneid, P. Sreekumar, and D. J. Thompson, “EGRET observations of high-energy Gamma-ray emission from blazars: An update”, *Astrophys. J.* **490** 116–135 (1997).
 7. L. S. The, D. D. Clayton, J. Jin, and B. S. Meyer, “Nuclear reactions governing the nucleosynthesis of ^{44}Ti ”, *Astrophys. J.* **504**, 500–515 (1998).
 8. A. F. Iyudin, V. Schonfelder, K. Bennett, H. Bloemen, R. Diehl, W. Hermsen, W., G. G. Lichti, R. D. van der Meulen, J. Ryan, and C. Winkler, “Emission from ^{44}Ti associated with a previously unknown galactic supernova”, *Nature* **396**, 142-144 (1998).
 9. F. X. Timmes and S. E. Woosley, “Gamma-ray line signals from supernovae within 100 MPC”, *Astrophys. J.* **489**, 160–169 (1997).
 10. R. D. Blandford and J. P. Ostriker, “Particle acceleration by astrophysical shocks”, *Ap. J. (Letters)* **221**, L29–L32, (1978).
 11. A. R. Bell, “The acceleration of cosmic rays in shock fronts. II”, *M. N. R. A. S.* **182**, 443–455 (1978).

12. S. P. Reynolds, “Models of synchrotron X-rays from shell supernova remnants”, *Astrophys. J.* **493**, 375–396 (1998).
13. R. L. Kinzer, W. R. Purcell, and J. D. Kurfess, “Gamma-ray emission from the inner galactic ridge”, *Astrophys. J.* **515**, 215–225 (1999).
14. M. A. McLaughlin, J. M. Cordes, and M. P. Ulmer, “Gamma-ray pulsar luminosities”, in *AIP Conf. Proc. 410: Proceedings of the Fourth Compton Symposium* **410**, 633–637 (1997).
15. M. A. McLaughlin, & J. M. Cordes, “The Gamma-ray pulsar population”, *Astrophys. J.* **538**, 818–830 (2000).
16. M. Isenberg, D. Q. Lamb, and J. C. L. Wang, “Effects of the geometry of the line-forming region on the properties of cyclotron resonant scattering lines”, *Astrophys. J.* **505**, 688–714 (1998).
17. C. Kouveliotou, T. Strohmayer, K. Hurley, J. van Paradijs, M. H. Finger, S. Dieters, P. Woods, C. Thompson, and R. C. Duncan, “Discovery of a magnetar associated with the soft gamma repeater SGR 1900+14”, *Ap. J. (Letters)* **510**, L115–L118 (1999).
18. K. Hurley, C. Kouveliotou, P. Woods, E. Mazets, S. Golenetskii, D. D. Frederiks, T. Cline, and J. van Paradijs, “Precise interplanetary network localization of a new soft gamma repeater, SGR 1627-41”, *Ap. J. (Letters)* **519**, L143–L145 (1999).
19. C. Thompson and R. C. Duncan, “The soft gamma repeaters as very strongly magnetized neutron stars. II. Quiescent neutrino, X-Ray, and Alfvén wave emission”, *Astrophys. J.* **473**, 322–342 (1996).

20. M. C. Weisskopf, B. Brinkman, C. Canizares, G. Garmire, S. Murray, and L. P. van Speybroeck, “An overview of the performance and scientific results from the Chandra X-ray observatory”, *Pub. A.S.P.* **114**, 1–24 (2000).
21. W. W. Craig, C. J. Hailey, M. Jiminez-Garate, D. L. Windt, F. A. Harrison, P. Mao, F. E. Christensen, and A. M. Husain, “Development of thermally formed glass optics for astronomical hard X-Ray telescopes”, *Optics Express* **7**, 178–185 (2000).
22. S. E. Romaine, A. Ivan, R. J. Brun, F. E. Christensen, F. A. Harrison, W. W. Craig, and P. Gorenstein, “Multilayer optics for hard x-ray astronomy”, in *X-Ray Optics, Instruments, and Missions, IV*, R. B. Hoover and A. B. C. Walker, eds., *Proc. SPIE* **4138**, 120–125 (2000).
23. M. P. Ulmer, R. Altkorn, A. Madan, M. Graham, Y.-W. Chung, A. S. Krieger, C. Liu, B. P. Lai, D. C. Mancini, and P. Z. Takacs, “Fabrication of Wolter I multilayer coated optics via electroforming: an update”, in *X-Ray Optics Design, Performance, and Applications*, A. M. Khounsary, A. K. Freund, T. Ishikawa, G. Srajer, and J. Lang, eds., *Proc. SPIE* **3773**, 113–121 (1999).
24. D. Li, E. Cutiongco, E., Y.-W. Chung, M.-S. Wong, and W. D. Sproul, “Review of synthesis and characterization of amorphous carbon nitride thin films”, *Diamond Films and Technology* **5**, 261–273 (1995).
25. P.Z. Takacs, Brookhaven National Laboratory, 20 North Technology St., Upton NY, 11973, private communication (2002).
26. D. S. Windt, “IMD - Software for modeling the optical properties of multilayer

films”, *Computers in Physics* **12**, 360–370 (1998).

List of Figure Captions

Fig 1. Schematic of mandrel and principal coatings. The electroless-nickel-coated aluminum mandrel was supplied by Hyperfine Corp. All other coatings were deposited at Northwestern University.

Fig 2. Photograph of multilayer coated IEMP mirror following removal from mandrel and trimming.

Fig 3. Reflectivity at 30 keV. Solid line shows experimental results. Broken line shows theoretical reflectivity for model multilayer (see text).

Fig 4. Reflectivity at 10 keV (2 rotated mirror positions). Solid lines show experimental results. Broken line show theoretical reflectivity for model multilayer (see text).

Fig 5. The diffuse scattering intensity image obtained with a CCD. The vertical columns of the CCD pixels correspond to different scattering angles as indicated by the top horizontal axis. Also superposed is a plot of the integrated intensity profile. The inset shows the schematic representation of the diffused scattering from the curved surface. The incident angle, θ , is defined from the "average" surface, indicated by the dashed line.

Fig 6. An optical profiler scan of a segment cut from mirror 1 (see text) along the optical axis averaged over 55 microns in the direction perpendicular to the optical axis.

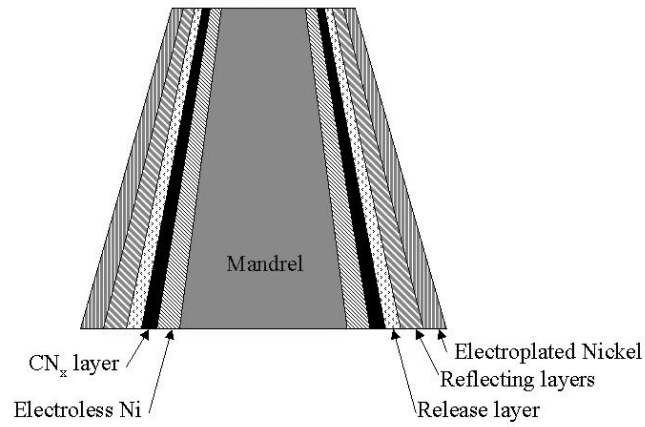


Fig. 1. Schematic of mandrel and principal coatings. The electroless-nickel-coated aluminum mandrel was supplied by Hyperfine Corp. All other coatings were deposited at Northwestern University

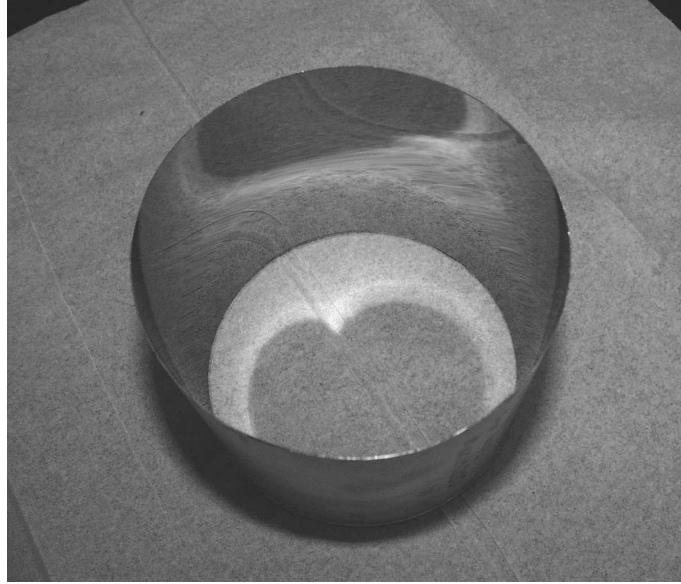


Fig. 2. Photograph of multilayer coated IEMP mirror following removal from mandrel and trimming.

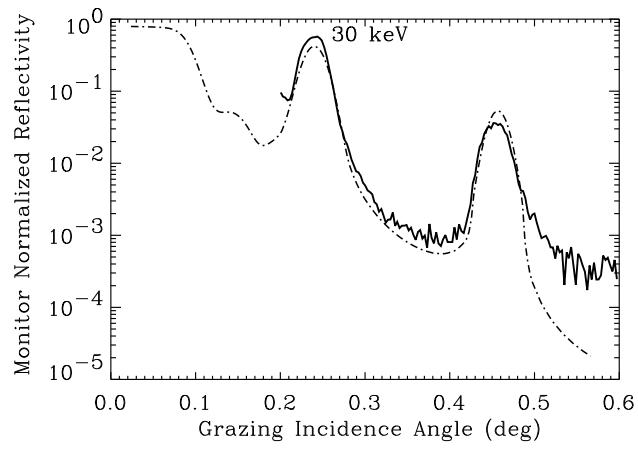


Fig. 3. Reflectivity at 30 keV. Solid line shows experimental results. Broken line shows theoretical reflectivity for model multilayer (see text)

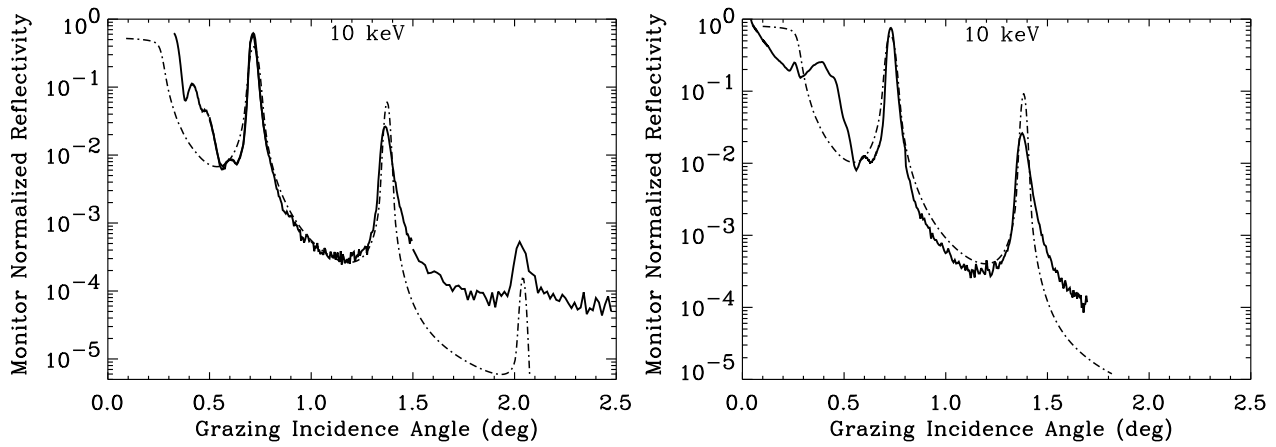


Fig. 4. Reflectivity at 10 keV (2 rotated mirror positions). Solid lines show experimental results. Broken line show theoretical reflectivity for model multilayer (see text).

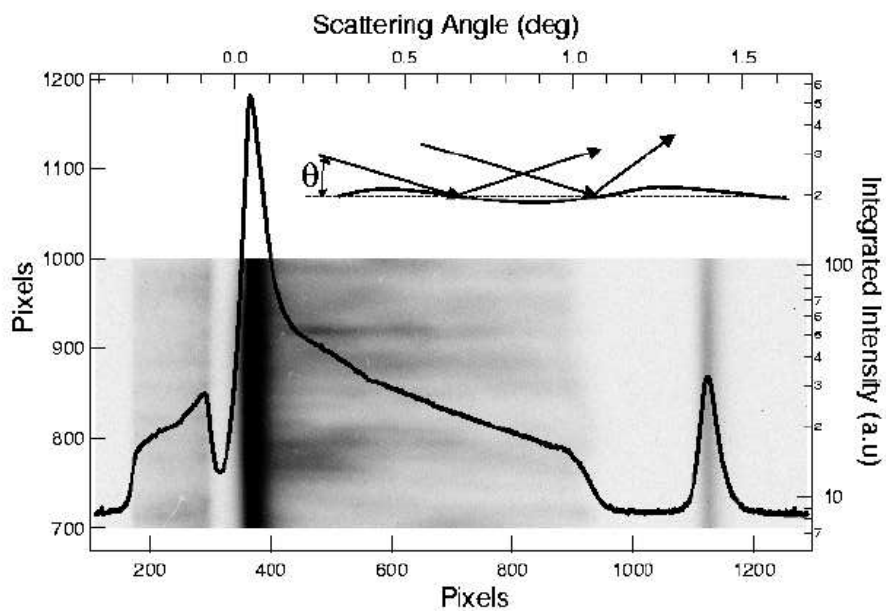


Fig. 5. The diffuse scattering intensity image obtained with a CCD. The vertical columns of the CCD pixels correspond to different scattering angles as indicated by the top horizontal axis. Also superposed is a plot of the integrated intensity profile. The inset shows the schematic representation of the diffused scattering from the curved surface. The incident angle, θ , is defined from the "average" surface, indicated by the dashed line.

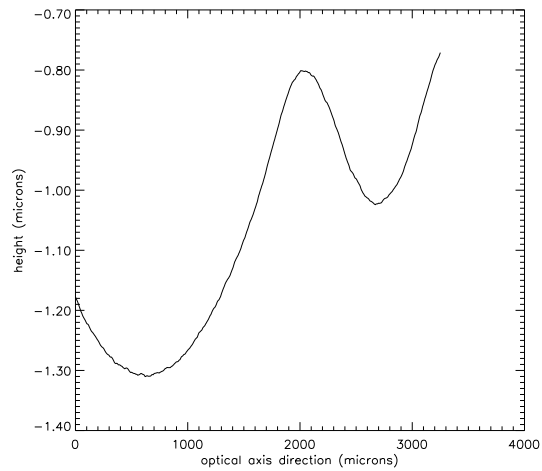


Fig. 6. An optical profiler scan of a segment cut from mirror 1 (see text) along the optical axis averaged over 55 microns in the direction perpendicular to the optical axis.